

Geometric phase mediated topological transport of sound

Shubo Wang^{1,2}, Guancong Ma¹, and C. T. Chan^{1*}

¹*Department of Physics, The Hong Kong University of Science and Technology, Hong Kong, China*

²*Department of Physics, City University of Hong Kong, Hong Kong, China*

* Correspondence to C. T. Chan (phchan@ust.hk)

Abstract

When a dynamic system undergoes a cyclic evolution, a geometric phase that depends only on the path traversed in parameter space can arise in addition to the normal dynamical phase. Such geometric phases have profound impacts in both quantum and classical physics. In classical systems, the geometric phase effect is commonly associated with the polarizations of vector waves, which are absent in scalar wave systems. Here, by exploiting the orbital angular momentum of sound vortices as a new degree of freedom, we successfully observed the geometric phase effect in airborne sound, which is a scalar wave. We show with both theory and experiments that these effects, associated with the helical transportation of sound, can be used to control the flow of sound vortices. This finding opens new possibilities for the manipulation of scalar wave propagation by exploiting geometric phases.

The concept of geometric phase applies to state evolutions in both classical¹ and quantum-mechanical systems². Consider a Hamiltonian $H(\lambda)$, which depends smoothly on the parameter λ as in $H(\lambda)\Psi = E(\lambda)\Psi$, where $E(\lambda)$ is the non-degenerate eigenvalue. For the adiabatic evolution of the Hamiltonian with respect to the parameter λ , the variation of λ can induce a coupling between a fast and a slow variable of the system. By separately treating the two variables as in the Born-Oppenheimer approximation, the dynamics of the fast variable can induce an effective vector potential (the curl of which defines an effective magnetic field) acting on the slow dynamic motion of the system³. Such a vector potential contributes to a phase factor that corresponds to the U(1) Abelian gauge field and is essentially the holonomy that characterizes the twisting of a Hermitian line bundle over parameter space⁴, which is the geometric phase. In the case of degenerate eigenvalues, the adiabatic evolution can give rise to a non-Abelian gauge structure⁵. In addition to fruitful applications in quantum-mechanical systems⁶, the geometric phase concept becomes increasingly popular in classical systems, such as for electromagnetic waves^{7–13}. Related experimental observations of such a phase have been achieved using twisted optical fibres^{14,15}, wave plates^{16–18} and meta-surfaces^{19–21}.

In electromagnetic wave systems, the intrinsic spin or orbital angular momentum (OAM) may play the role of the fast variable. Its interaction with the extrinsic linear orbital momentum \mathbf{k} can modify the propagation dynamics of a beam field, resulting in the photonic analogue of spin/orbital Hall effect^{15,19,22–24}. In this paper, we show that a similar geometric phase effect can also be realized with airborne sound. In contrast to electromagnetic waves, sound propagates in fluids as a longitudinal scalar wave. The absence of a polarization vector means that sound cannot give rise to geometric phases through the spin degree of freedom. However, a sound wave can carry OAM in the form of a sound vortex^{25–28}, which provides a new degree of freedom for

the manifestation of the geometric phase effect. We show that the transport of sound vortices inside a helical waveguide induces geometric phases that can affect the transmission properties. These phenomena can be viewed as a consequence of the coupling between the orbital angular momentum and the linear momentum induced by helical transport.

Geometric phase induced by helical transportation of sound vortices

We consider a circular waveguide of radius a filled with air. Sound propagating inside the waveguide is governed by the wave equation $c^2 \nabla^2 P(\mathbf{r}, t) = \partial^2 P(\mathbf{r}, t) / \partial t^2$, where c is the sound speed and $P(\mathbf{r}, t)$ is the pressure field. By defining the operator $\hat{H} = c^2 \nabla^2$, the wave equation can be rewritten as $\hat{H}P(\mathbf{r}, t) = \partial^2 P(\mathbf{r}, t) / \partial t^2$. Using cylindrical coordinates (r, φ, z) and the separation of variables, one can obtain the solutions to the wave equation for the cylindrical waveguide in the form of $J_l(k_r r)(A \cos l\varphi + B \sin l\varphi)e^{ik_z z} e^{i\omega t}$ ²⁹, where $J_l(k_r r)$ is the l th-order cylindrical Bessel function of the first kind; k_r and k_z are the transverse and longitudinal wavenumber, respectively; and A and B are arbitrary coefficients. Since the radial particle velocity at $r = a$ is zero, the Dirichlet boundary condition $[\partial J_l(k_r r) / \partial r]_{r=a} = 0$ is applied to determine the discrete guided modes. These modes can be labelled by (m, l) with m denoting the m^{th} root. Figure 1 shows the dispersion relations of the three lowest-order modes with the corresponding mode pressure field. The monopole mode has a homogeneous pressure distribution along the transverse plane and, hence, the pressure variation is purely longitudinal. The pressure fields of higher-order modes, such as the dipole mode, have non-uniform phases on the transverse plane and therefore can be assigned a transverse polarization, so that the guided sound modes can be viewed as “transversely” polarized²⁹. We note that the solutions to the wave

equation can be expanded using the complete basis $\{J_l(k_r r) e^{il\phi} e^{ik_z z}\}$. For the partial waves with $m=0$ and $l \neq 0$, $J_l(k_r r) e^{il\phi} e^{ik_z z}$ denotes a vortex field of topological charge $q=l$ that carries an OAM of $l\hbar$ per quanta. A sound vortex with $q=+1$ can be excited using 4 monopole sources with an azimuthal phase gradient of $\pi/2$ at one end of the waveguide, as shown by the inset of Fig. 1, where the excited pressure field is plotted. Such a sound vortex can also be excited using a transducer array^{25,30}, a metasurface^{27,28} or resonance structures²⁶. A sound vortex with an opposite charge of $q=-1$ can be excited by simply reversing the phase gradient of the monopole sources.

Now, we bend the straight waveguide into a helix of radius R and pitch D , as shown in Fig. 2a. The helical structures have been widely used in electromagnetics (such as antennae³¹ and travelling-wave tube³²) and in photonics and plasmonics^{33–35}. However, the helical transport of sound remains largely unexplored. The helical bending effectively induces a rotation of the local coordinate frame $(\mathbf{u}, \mathbf{v}, \mathbf{t})$ attached to the waveguide, where \mathbf{t} denotes the unit tangent vector that forms an angle θ with the laboratory z axis. Therefore, under adiabatic conditions, the wave undergoes the transformation $P' = \hat{R}(\mathbf{n}, \phi)P$, where $\hat{R}(\mathbf{n}, \phi) = e^{-i\phi\hat{L}\cdot\mathbf{n}}$ is the unitary rotation operator that applies a rotation of angle ϕ on P with respect to the axis \mathbf{n} . $\hat{L} = -i\mathbf{r} \times \nabla$ is the OAM operator that serves as the generator of the rotation. The time evolution of the vortices can be expressed as (see Methods)

$$\frac{\partial^2 P'}{\partial t^2} = \left[\hat{H} + 2\omega\hat{L}\cdot\mathbf{\Omega} - (\hat{L}\cdot\mathbf{\Omega})^2 \right] P', \quad (1)$$

where in the laboratory frame we have $\hat{L}\cdot\mathbf{\Omega} = \mathbf{t}\cdot\hat{L}\Omega(\cos\theta - 1)$ and $\mathbf{\Omega} = \partial\phi/\partial t$. Using the relationship $\hat{p} = -i\nabla$, the operator for the helical waveguide can be expressed formally as

$$\hat{H}'(\mathbf{k}) = -c^2 \left(\hat{p} - \mathbf{a} \hat{L} \cdot \mathbf{k} \right)^2, \quad (2)$$

where $\alpha = |\mathbf{a}| = (\cos \theta - 1) \sin \theta c / (R\omega)$ and \mathbf{a} is in the same direction as \hat{p} ; and $\mathbf{k} = k\mathbf{t}$ is the longitudinal wave vector inside the waveguide. The corresponding eigen frequency is

$$\omega' = \omega - c\alpha k. \quad (3)$$

If we view the helical waveguide as a periodic structure, the longitudinal wave vector \mathbf{k} in equation (2) can be mapped to the Bloch wave vector $\mathbf{k}_B = k_B \hat{z}$ with $k = (D/S)k_B$, where S is the total length of the helical waveguide for one pitch (see Supplementary Information). In the limit of $a \ll R, D$, we have $S \approx \sqrt{D^2 + (2\pi R)^2} = D / \cos \theta$ and, hence, the operator in equation (2) can also be expressed as $\hat{H}'(\mathbf{k}_B) = -c^2 \left(\hat{p} - \mathbf{a} \hat{L} \cdot \mathbf{k}_B \right)^2$. The second term inside the parentheses of \hat{H}' represents the contribution from an l -dependent synthetic gauge potential induced by the helical structure of the waveguide. Such a synthetic gauge potential induces a coupling between the OAM and the linear momentum. The OAM- \mathbf{k}_B interaction lifts the spectral degeneracy of the $\pm q$ vortices, as shown in Fig. 2b for a prototypical system with $a = 3.25$ cm, $R = 32.5$ cm and $D = 65$ cm. The circles denote the full-wave numerical results obtained using the finite-element package COMSOL³⁶. The solid lines denote the analytical results obtained using equation (3), which are folded into the first Brillouin zone by using the mapping $k = (D/S)k_B$ (see Supplementary Information for details). The monopole band is not of interest and is thus not shown here. We notice a good match between the analytical and numerical results for the sound vortices $q = \pm 1$. For the straight waveguide, the $q = \pm 1$ vortices are degenerate while this degeneracy is lifted in the helical waveguide. This can also be interpreted as a lateral shift of the bands along opposite directions of \mathbf{k}_B due to the OAM- \mathbf{k}_B coupling in presence of a synthetic

gauge potential, analogous to the spin-orbit interaction in solid-state materials and cold-atom systems³⁷.

The above phenomenon can also be explained using the Berry phase picture introduced to address the adiabatic evolution of states, which has well-known examples in quantum-mechanical systems². For the helical waveguide with a smooth bending feature, the eigen wave equation can be expressed as

$$-c^2 \left[\hat{p} - \mathbf{a} \hat{L} \cdot \mathbf{k}(\xi) \right]^2 |\mathbf{k}(\xi), l\rangle = -\omega'^2 |\mathbf{k}(\xi), l\rangle. \quad (4)$$

Here, we use $|\mathbf{k}(\xi), l\rangle$ to denote the vortex state and ξ is a variable characterizing the position of the vortex inside the waveguide. The above equation is formally analogous to the governing equation of the electron spin evolution under a slowly varying magnetic field, which is expressed as $g \mathbf{s} \cdot \mathbf{B}(t) |\mathbf{B}(t), m_s\rangle = E |\mathbf{B}(t), m_s\rangle$, where g is the gyromagnetic ratio; \mathbf{s} is the electron spin; and m_s is the spin projection along the direction of the magnetic field $\mathbf{B}(t)$. Therefore, one can similarly define a Berry connection³⁸

$$\mathbf{A}(\mathbf{k}) = -i \langle \mathbf{k}(\xi), l | \nabla_{\mathbf{k}} | \mathbf{k}(\xi), l \rangle = -\frac{l}{k} \cot \theta \hat{\phi}, \quad (5)$$

where $\hat{\phi}$ is the unit direction vector of the azimuthal coordinate ϕ . The corresponding Berry curvature is simply $\mathbf{F}(\mathbf{k}) = \nabla_{\mathbf{k}} \times \mathbf{A}(\mathbf{k}) = l \mathbf{k} / k^3$ ³⁸, which represents an effective magnetic monopole at the origin of momentum space. The geometric phase can be obtained as an integral of the Berry connection over the traversed path C in momentum space as shown in Fig. 2c. This gives $\Phi = l \int (1 - \cos \theta) d\phi$ in the laboratory frame³⁸ and is proportional to the solid angle subtended by C . We note that the geometric phase agrees with equation (3), which provides an accumulated phase after time dt :

$$\Phi = - \int c \alpha l k dt = l \int (1 - \cos \theta) d\phi. \quad (6)$$

Visualizing the geometric phase effect

To visualize the acoustic geometric phase effect, we performed experiments of sound vortex transport inside a waveguide, as shown in Fig. 3 (see Methods for details). A sound vortex with $q = +1$ was excited at one end of the waveguide using mini loudspeakers arranged in the same way as in Fig. 1. We measured the output pressure magnitude and phase by a microphone at the other end. Figure 3a, d shows the setup and measured results of the straight cylindrical waveguide. We see that the pressure magnitude has a donut shape with a phase singularity at the centre, which are clear signatures of a vortex. Figure 3b shows the same waveguide gently bent on the vertical plane. The resulting pressure field (Fig. 3e) is identical to that of the straight waveguide. This is because the trajectory of the vortex state covers zero area on the sphere in momentum space (Fig. 2c); hence, no geometric phase is induced. When the same waveguide is twisted into a single pitch helix with $\theta = \cos^{-1}(3/4)$, resulting in a 3D configuration as shown in Fig. 3c, the phase profile of the output pressure field (Fig. 3f) clearly shows a rotation compared to the straight and bent case. This is a manifestation of the geometric phase $\Phi = \pi/2$. We note that for a vortex of $q = -1$ with an opposite OAM, the induced geometric phase has an opposite sign.

The observed phenomenon may be viewed as the acoustic analogue of circular birefringence induced by geometric phases. When a linearly polarized dipole mode of the form $e^{i\phi_0} + e^{-i\phi_0}$, where ϕ_0 denotes the initial polarization direction, is excited at the input of the helical waveguide in Fig. 3c, the right- and left-handed components acquire opposite geometric phase

advances, leading to a rotation of the output pressure field by an angle of Φ as

$e^{i\phi_0} + e^{-i\phi_0} \rightarrow e^{i\phi_0}e^{i\Phi} + e^{-i\phi_0}e^{-i\Phi} = 2\cos(\phi_0 + \Phi)$. This rotation effect is demonstrated through the experimental and full-wave numerical results shown in Fig. 4. We see that, compared with the input field magnitude, the output field magnitude is rotated approximately by $\pi/2$, in good agreement with the results of Fig. 3c and the analytical results predicted by equation (6). The experimental results are also in good agreement with the full-wave simulation results.

Sound vortex interferometer

Controlling the transmission of vortex states is useful for applications such as OAM multiplexing, which can improve communication bandwidth^{39,40}. To demonstrate that the geometric phase can be used to manipulate sound vortex transmissions, we construct an acoustic interferometer as shown in Fig. 5a. The system consists of two waveguides of the same cross-sectional shape. One waveguide is a slightly bent but lies flat on a 2D plane as is defined by the table top. The other waveguide forms a two-pitch helix. The two waveguides meet at two ends and are connected to straight waveguides of the same cross-sectional shape for the input and detection. We excited sound vortices with $q = \pm 1$ at the left input and measured the pressure field at the right output, as shown in Fig. 5a. To characterize the transmission difference between the $q = +1$ and $q = -1$ vortices, we define the parameter $\eta = |t_+ - t_-| / |t_+ + t_-|$, where $t_{\pm} = \int |p_{\pm}|^2 dA$ denotes the integral of the square of the pressure field magnitude over the output cross-sectional area for the $q = \pm 1$ vortices. The t_+ and t_- are not generally the same because the $q = \pm 1$ vortices acquire different geometric phases after passing through the helical waveguide. The maximum difference between t_+ and t_- is achieved when constructive interference occurs to

one vortex while destructive interference occurs to the opposite vortex. The measured results are plotted in Fig. 5b as red dots connected by lines, where we observe a dramatic variation in η . In Fig. 5c, we show the output pressure profiles for the $q = +1$ (upper panel) and $q = -1$ (lower panel) vortices at the frequency of 3,295 Hz, where η reaches a peak. At this point, we see that the two pressure profiles are quite different. For the $q = +1$ input, the output pressure distribution resembles a distorted vortex of the same charge. For the $q = -1$ input, the output is dominated by a monopole field. The emerging of the monopole field is attributed to the symmetry-breaking-induced mode conversion at the branch nodes where the two waveguide branches merge.

For comparison, we performed another measurement in which the same helical waveguide (Fig. 5a) is unwound and lies flat on the same 2D plane defined by the table top. We repeated the measurement with both the $q = +1$ and $q = -1$ input vortices. According to previous analysis, sound vortices acquire no geometric phase propagating through this 2D system. The parameter η for this 2D system is plotted in Fig. 5b in blue. In stark contrast to the 3D system with a helical waveguide, it is clearly seen that η remains close to zero throughout. This means that the interference spectra are the same for the $q = +1$ and $q = -1$ vortices, as a consequence of the zero geometric phase. In Fig. 5d, we also show the output pressure profiles at 3,295 Hz for the $q = +1$ (upper panel) and $q = -1$ (lower panel) vortices. The two patterns are clearly the mirror images of each other, which is due to the sign of the vortex charge. The output pressure profiles for the peak at approximately $f = 3,230$ Hz (Fig. 5b) have similar features and are shown in the Supplementary Fig. 2.

It is not easy to precisely parameterize the bending of the waveguide in our experimental system. We performed full-wave simulations for a similar system, and the results are

qualitatively the same as the experiment (see Supplementary Fig. 3), and lead to the same conclusion.

The geometric phase effects manifest in classical wave systems in various ways and are defined over different parameter spaces. For example, the manipulation of wave fronts using metasurfaces can be elegantly interpreted as locally induced geometric phases as a result of polarization change induced by subwavelength resonators. The parameter space for such metasurface systems is defined by the Poincare sphere of polarizations. In photonic or phononic topological insulators, the Brillouin zone serves as the parameter space where a quantized geometric phase can be defined for each discrete band, leading to integral values of topological invariants that can be used to predict the existence and the number of boundary modes. The quantized geometric phase determines the global topological structure of the Bloch wavefunctions indexed by the Bloch wavevector on the Brillouin torus. In our study, the parameter space is defined by the wave vector \mathbf{k} and the geometric phase is induced by the nontrivial winding of \mathbf{k} . Such a geometric phase is very general and exists in wave scattering or focusing⁴¹. For electromagnetic waves, which are transverse waves, the $\mathbf{k} \cdot \mathbf{E} = 0$ condition guarantees that the polarization direction must accompany the rotation of \mathbf{k} , and the geometric phase effects arise naturally. Here, we show that sound, as a longitudinal scalar wave, manifests similar geometric phase effect thanks to its OAM evolution inside a helical waveguide.

In summary, we theoretically and experimentally demonstrated that airborne sound, as a scalar longitudinal wave, can have geometric phase effects when it travels inside helical waveguides. The geometric phase can be understood as a consequence of non-commutative SO(3) rotations or as a result of the adiabatic evolution of the vortex states in the wave vector space. The geometric phase has opposite sign for sound vortices with opposite orbital angular

momentum, leading to different transport properties. Such a geometric phase gives rise to the rotation of the sound pressure field on the transverse plane. The effect can also be considered as an acoustic analogue of circular birefringence. Using an interferometer structure, we manipulated the transmission spectrum of sound vortices based on the geometric phase effect. These results demonstrate that, although sound is a scalar wave without spin, the orbital angular momentum of sound can also have interesting topological properties that may find applications in the manipulations of sound signals.

Methods

Wave equation for the helical waveguide. The wave equation for the straight waveguide is $\hat{H}P(\mathbf{r},t) = \partial^2 P(\mathbf{r},t) / \partial t^2$, where $\hat{H} = c^2 \nabla^2$. For sound propagating inside a helical waveguide, the wave undergoes an effective rotation of $P' = \hat{R}(\mathbf{n},\phi)P$, where $\hat{R}(\mathbf{n},\phi) = e^{-i\phi\hat{L}\cdot\mathbf{n}}$ is the rotation operator and $\hat{L} = -i\mathbf{r} \times \nabla$ is the OAM operator. The time evolution of the wave state can be expressed as

$$\begin{aligned}
\frac{\partial^2 P'}{\partial t^2} &= \frac{\partial}{\partial t} \left(\hat{R} \frac{\partial P}{\partial t} + \frac{\partial \hat{R}}{\partial t} P \right) \\
&= \frac{\partial}{\partial t} \left(\hat{R} \frac{\partial P}{\partial t} - i\hat{L} \cdot \mathbf{\Omega} \hat{R} P \right) \\
&= \left[\hat{R} \frac{\partial^2 P}{\partial t^2} - 2i\hat{L} \cdot \mathbf{\Omega} \hat{R} \frac{\partial P}{\partial t} - (\hat{L} \cdot \mathbf{\Omega})^2 \hat{R} P \right] \\
&= \left[\hat{R} \hat{H} \hat{R}^\dagger + 2\omega \hat{L} \cdot \mathbf{\Omega} - (\hat{L} \cdot \mathbf{\Omega})^2 \right] P',
\end{aligned} \tag{7}$$

where we have used $\hat{H}P = \partial^2 P / \partial t^2$ and $\partial P / \partial t = i\omega P$. Therefore, the operator for the helical waveguide is simply $\hat{H} + 2\omega \hat{L} \cdot \mathbf{\Omega} - (\hat{L} \cdot \mathbf{\Omega})^2$, assuming rotational invariance $\hat{H} = \hat{R} \hat{H} \hat{R}^\dagger$. In the

laboratory frame, we have $\hat{L} \cdot \Omega = \mathbf{t} \cdot \hat{L} \Omega (\cos \theta - 1)$, where $\Omega = \partial \phi / \partial t = \sin \theta v_g / R$ with $v_g = \partial \omega / \partial k = c^2 k / \omega$ being the group velocity of the wave inside the waveguide. Using the definition of the momentum operator $\hat{p} = -i\nabla$, the final expression for the operator can be rewritten as

$$\hat{H}'(\mathbf{k}) = -c^2 \left(\hat{p} - \mathbf{a} \hat{L} \cdot \mathbf{k} \right)^2, \quad (8)$$

where $\alpha = |\mathbf{a}| = (\cos \theta - 1) \sin \theta c / (R\omega)$ and \mathbf{a} has the same direction as \hat{p} ; and $\mathbf{k} = k\mathbf{t}$ is the longitudinal wave vector of the sound vortices. The second term in the brackets can be understood as a synthetic gauge potential. The corresponding eigen frequency is

$$\omega' = \omega - c\alpha k. \quad (9)$$

Note that we have assumed adiabatic conditions in the above formulations and Bragg scattering effects are not included.

Numerical simulations. The full-wave numerical simulations are performed using the finite-element package COMSOL Multiphysics³⁶. All the waveguides have radii of $r = 3.75$ cm in accordance with the experimental setup. For the excitation of the $q = +1$ vortex in Fig. 1 and the simulated rotation effect in Fig. 4, the vortex is excited at one end of the waveguide using four monopole sources arranged on a circle of radius $r = 2.25$ cm. The radiation boundary condition is set at the output end. For the band structure calculations in Fig. 2b, one pitch of the helix is employed with $R = 32.5$ cm, $D = 65$ cm, and periodic boundary condition is applied on both ends.

Experiments. The waveguides used in the experiments are polymer tubes, which is slightly flexible so that it can be bent into curved shapes. The wall of the tube is reinforced by steel wire, so that it can retain its circular cross-sectional shape when bent. Four mini-loudspeakers are connected to four phase-locked signal generators to excite the sound vortices with $q = \pm 1$. To measure the output pressure field, a miniature microphone is mounted on a motorized translational stage to scan the cross section of the waveguide at the output. The radius of the waveguide cross section is $r = 3.75$ cm. The radius and pitch of the helix waveguide in Fig. 3c are $R = 32.5$ cm and $D = 2\pi R \cot \theta$ with $\theta = \cos^{-1}(3/4)$, respectively.

Data availability

The data that support the plots within this paper and other findings of this study are available from the corresponding author on request.

Acknowledgements

This work was supported by AoE/P-02/12. We thank Prof. Z. Q. Zhang for valuable comments and suggestions. S. W. is also supported by a grant from City University of Hong Kong (Project No. 7200549).

Author contributions

S.W. performed the numerical simulations and analytical calculations. G.M. designed and carried out the experiments. S.W. and G.M. contributed equally to this work. C.T.C. supervised the project. All authors contributed to the discussions and the shaping of the manuscript.

Competing financial interests

The authors declare no competing financial interests.

References

1. Pancharatnam, S. Generalized theory of interference, and its applications. *Proc. Indian Acad. Sci. - Sect. A* **44**, 247–262 (1956).
2. Berry, M. V. Quantal phase factors accompanying adiabatic changes. *Proc. R. Soc. Lond. Math. Phys. Eng. Sci.* **392**, 45–57 (1984).
3. Jackiw, R. Three elaborations on Berry’s connection, curvature and phase. *Int. J. Mod. Phys. A* **03**, 285–297 (1988).
4. Simon, B. Holonomy, the quantum adiabatic theorem, and Berry’s phase. *Phys. Rev. Lett.* **51**, 2167–2170 (1983).
5. Wilczek, F. & Zee, A. Appearance of gauge structure in simple dynamical systems. *Phys. Rev. Lett.* **52**, 2111–2114 (1984).
6. Xiao, D., Chang, M.-C. & Niu, Q. Berry phase effects on electronic properties. *Rev. Mod. Phys.* **82**, 1959–2007 (2010).
7. Haldane, F. D. M. Path dependence of the geometric rotation of polarization in optical fibers. *Opt. Lett.* **11**, 730–732 (1986).
8. Segert, J. Photon Berry’s phase as a classical topological effect. *Phys. Rev. A* **36**, 10–15 (1987).
9. Samuel, J. & Bhandari, R. General setting for Berry’s phase. *Phys. Rev. Lett.* **60**, 2339–2342 (1988).
10. Kugler, M. & Shtrikman, S. Berry’s phase, locally inertial frames, and classical analogues. *Phys. Rev. D* **37**, 934–937 (1988).
11. Wilczek, F. *Geometric Phases in Physics* (World Scientific, Singapore, 1989).

12. Vinitskii, S. I., Derbov, V. L., Dubovik, V. M., Markovski, B. L. & Stepanovskii, Y. P. Topological phases in quantum mechanics and polarization optics. *Sov. Phys. Uspekhi* **33**, 403 (1990).

13. Biener, G., Niv, A., Kleiner, V. & Hasman, E. Formation of helical beams by use of Pancharatnam–Berry phase optical elements. *Opt. Lett.* **27**, 1875–1877 (2002).

14. Tomita, A. & Chiao, R. Y. Observation of Berry’s topological phase by use of an optical fiber. *Phys. Rev. Lett.* **57**, 937–940 (1986).

15. Bliokh, K. Y., Niv, A., Kleiner, V. & Hasman, E. Geometrodynamics of spinning light. *Nat. Photonics* **2**, 748–753 (2008).

16. Bhandari, R. & Samuel, J. Observation of topological phase by use of a laser interferometer. *Phys. Rev. Lett.* **60**, 1211–1213 (1988).

17. Marrucci, L., Manzo, C. & Paparo, D. Optical spin-to-orbital angular momentum conversion in inhomogeneous anisotropic media. *Phys. Rev. Lett.* **96**, 163905 (2006).

18. Milione, G., Evans, S., Nolan, D. A. & Alfano, R. R. Higher order Pancharatnam-Berry phase and the angular momentum of light. *Phys. Rev. Lett.* **108**, 190401 (2012).

19. Hosten, O. & Kwiat, P. Observation of the spin Hall effect of light via weak measurements. *Science* **319**, 787–790 (2008).

20. Li, G. *et al.* Spin-enabled plasmonic metasurfaces for manipulating orbital angular momentum of light. *Nano Lett.* **13**, 4148–4151 (2013).

21. Li, G. *et al.* Continuous control of the nonlinearity phase for harmonic generations. *Nat. Mater.* **14**, 607–612 (2015).

22. Onoda, M., Murakami, S. & Nagaosa, N. Hall effect of light. *Phys. Rev. Lett.* **93**, 083901 (2004).

23. Bliokh, K. Y. Geometrical optics of beams with vortices: Berry phase and orbital angular momentum Hall effect. *Phys. Rev. Lett.* **97**, 043901 (2006).

24. Ling, X., Zhou, X., Shu, W., Luo, H. & Wen, S. Realization of tunable photonic spin Hall effect by tailoring the Pancharatnam-Berry phase. *Sci. Rep.* **4**, 5557 (2014).

25. Demore, C. E. M. *et al.* Mechanical evidence of the orbital angular momentum to energy ratio of vortex beams. *Phys. Rev. Lett.* **108**, 194301 (2012).

26. Jiang, X., Li, Y., Liang, B., Cheng, J. & Zhang, L. Convert acoustic resonances to orbital angular momentum. *Phys. Rev. Lett.* **117**, 034301 (2016).

27. Jiang, X. *et al.* Broadband and stable acoustic vortex emitter with multi-arm coiling slits. *Appl. Phys. Lett.* **108**, 203501 (2016).

28. Ye, L. *et al.* Making sound vortices by metasurfaces. *AIP Adv.* **6**, 085007 (2016).

29. Hartig, H. E. & Swanson, C. E. ‘Transverse’ acoustic waves in rigid tubes. *Phys. Rev.* **54**, 618–626 (1938).

30. Anh äuser, A., Wunenburger, R. & Brasselet, E. Acoustic rotational manipulation using orbital angular momentum transfer. *Phys. Rev. Lett.* **109**, 034301 (2012).

31. Wheeler, H. A. A helical antenna for circular polarization. *Proc. IRE* **35**, 1484–1488 (1947).

32. Jr, A. S. G. *Principles of Traveling Wave Tubes* (Artech Print on Demand, Boston, 1994).

33. Pendry, J. B. A chiral route to negative refraction. *Science* **306**, 1353–1355 (2004).

34. Gansel, J. K. *et al.* Gold helix photonic metamaterial as broadband circular polarizer. *Science* **325**, 1513–1515 (2009).

35. Wang, S. B. & Chan, C. T. Lateral optical force on chiral particles near a surface. *Nat. Commun.* **5**, 3307 (2014).

36. www.comsol.com.

37. Galitski, V. & Spielman, I. B. Spin-orbit coupling in quantum gases. *Nature* **494**, 49–54 (2013).
38. Bliokh, K. Y., Rodríguez-Fortuño, F. J., Nori, F. & Zayats, A. V. Spin-orbit interactions of light. *Nat. Photonics* **9**, 796–808 (2015).
39. Bozinovic, N. *et al.* Terabit-scale orbital angular momentum mode division multiplexing in fibers. *Science* **340**, 1545–1548 (2013).
40. Shi, C., Dubois, M., Wang, Y. & Zhang, X. High-speed acoustic communication by multiplexing orbital angular momentum. *Proc. Natl. Acad. Sci.* **114**, 7250–7253 (2017).
41. Bliokh, K. Y. *et al.* Spin-to-orbital angular momentum conversion in focusing, scattering, and imaging systems. *Opt. Express* **19**, 26132–26149 (2011).

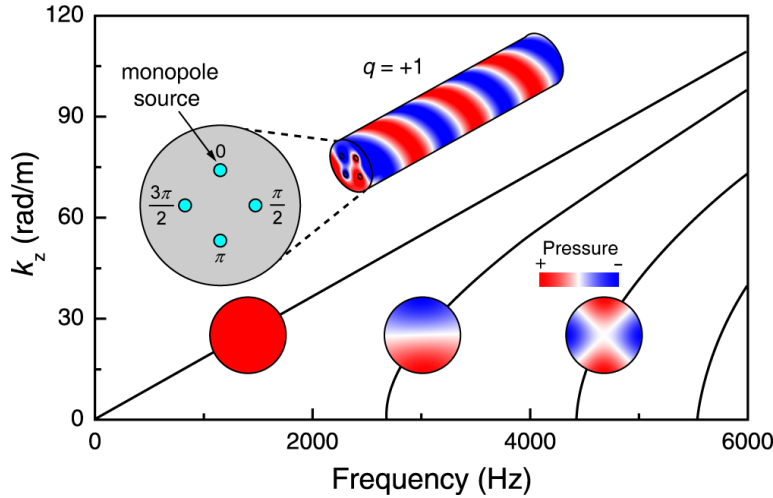


Figure 1 | Sound vortices inside a circular waveguide. The solid lines show the dispersion relations of the lowest-order guided modes (monopole, dipole and quadrupole), labelled by the corresponding mode pressure field. A vortex of charge $q = +1$ can be excited using four monopole sources with initial phases $0, \pi/2, \pi, 3\pi/2$, and the corresponding pressure field is shown in the insert. The vortex with $q = -1$ can be excited using monopole sources with a reversed order of arrangement.

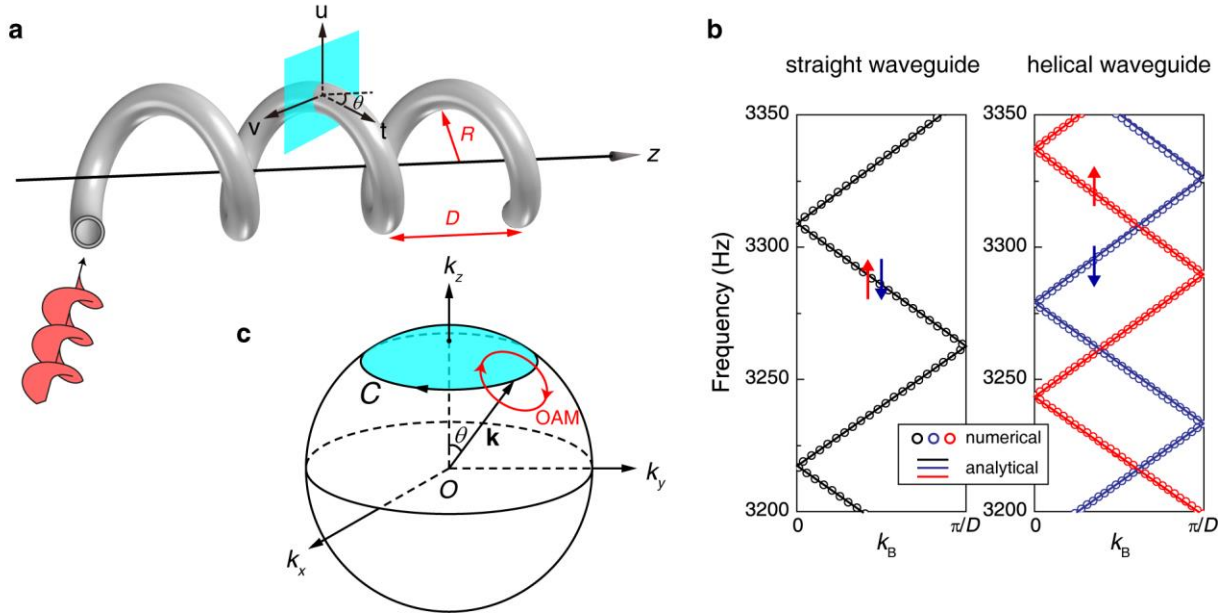


Figure 2 | Geometric phase induced by helical transportation of sound vortices. **a**, Sound vortices travelling through a helical waveguide acquire a geometric phase in addition to the normal dynamic phase. Such a phase can be considered as the result of the rotation of the local coordinate system ($\mathbf{u}, \mathbf{v}, \mathbf{t}$) attached to the waveguide. **b**, Band structures for a straight waveguide and a helical waveguide showing the degeneracy lifting of the $q = \pm 1$ vortices due to the coupling of the OAM and linear momentum. The monopole band is not shown. **c**, The degeneracy lifting can be attributed to the geometric phase induced by the evolution of the vortex states in wave vector space. The circulation direction of \mathbf{k} depends on the handedness of the helical waveguide. The red circle denotes the circulating direction of the OAM carried by the sound vortex.

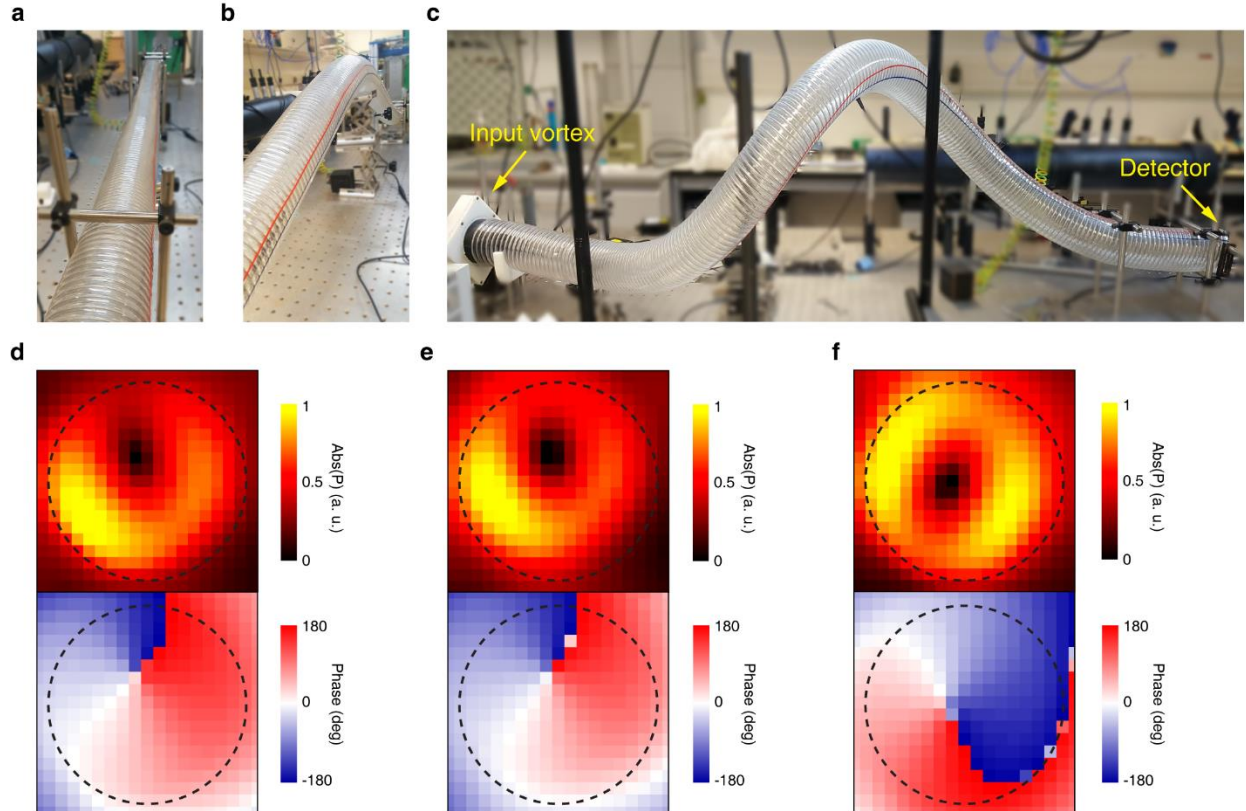


Figure 3 | Experimental demonstration of the geometric phase for a sound vortex. a-c, The Experimental setups for a straight waveguide, a bent waveguide, and a helical waveguide, respectively. **d-f,** The magnitude and phase of the pressure field detected at the end of the waveguide corresponding to a-c, respectively. The sound vortex is excited using a monopole source array at the input. The dashed circles denote the boundary of the waveguide cross section.

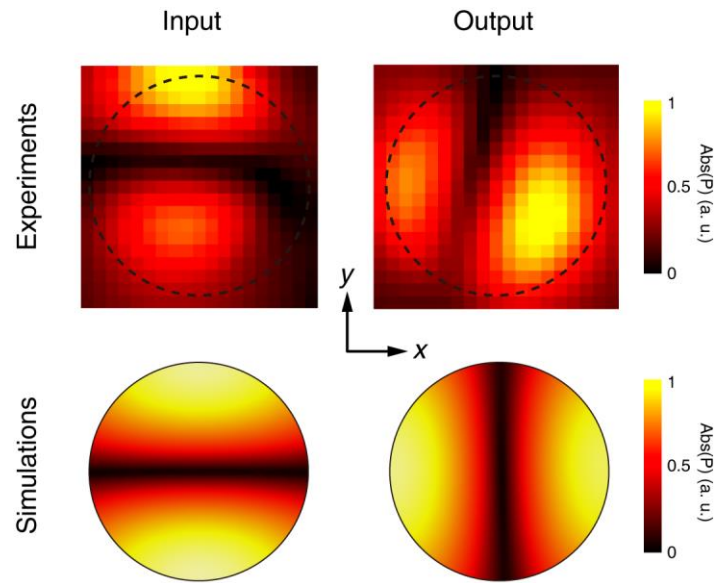


Figure 4 | Rotation effect induced by the geometric phase. Comparison between the experimental and full-wave simulation results for the normalized magnitude of the input and output pressure fields when a linear dipole mode along the y axis is excited. The system configuration is the same as in Fig. 3c.

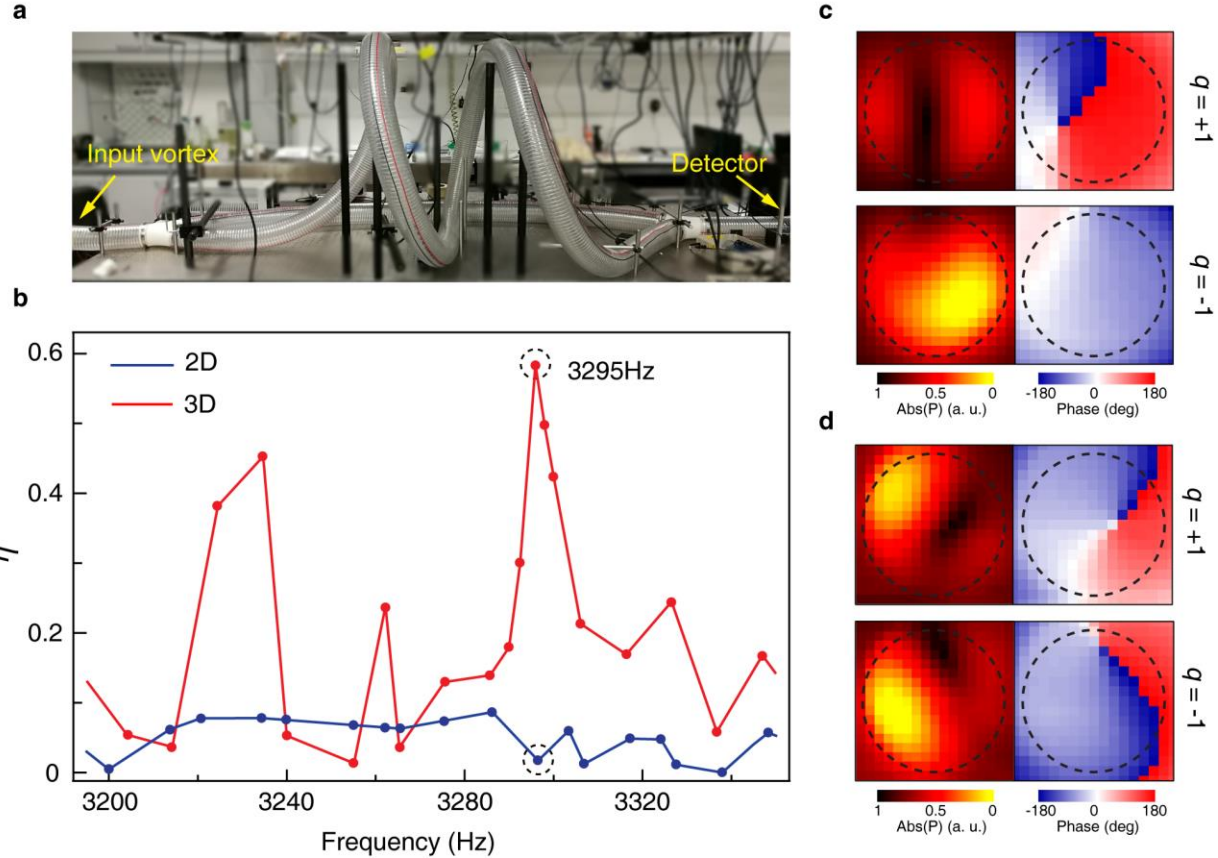


Figure 5 | Acoustic interferometer based on geometric phases. a, A 3D acoustic interferometer consisting of a helical waveguide and a bent waveguide. **b**, The transmission contrast η (see main text for definition) of the $q = \pm 1$ vortices as a function of frequency for the 2D (not shown) and 3D interferometers. The 2D setup is obtained by unwinding the helical waveguide so that the two waveguides lie on a 2D plane. **c**, The normalized magnitude and the phase of output pressure field of the $q = \pm 1$ vortices at the frequency $f = 3,295$ Hz for the 3D case. **d**, The normalized magnitude and the phase of the output pressure field of the $q = \pm 1$ vortices at the frequency $f = 3,295$ Hz for the 2D case, which has mirror symmetry.

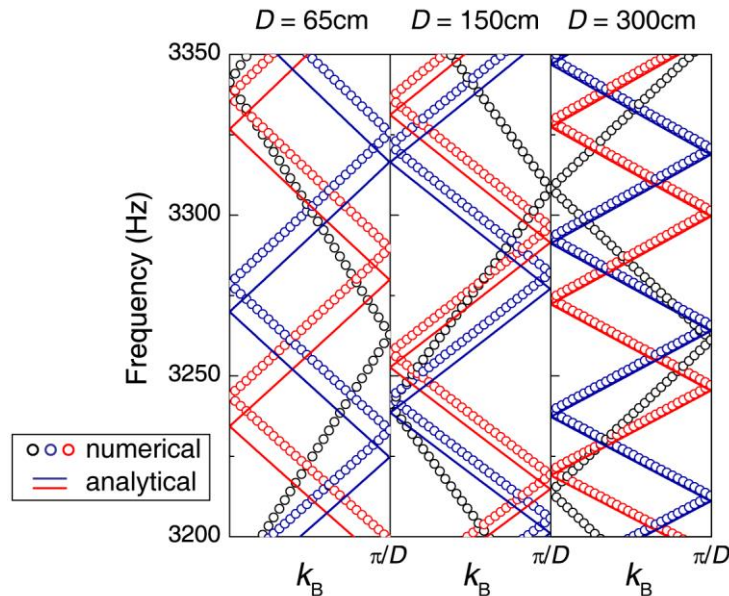
Supplementary Information for
Geometric phase mediated topological transport of sound

Shubo Wang^{1,2}, Guancong Ma¹, and C. T. Chan^{1*}

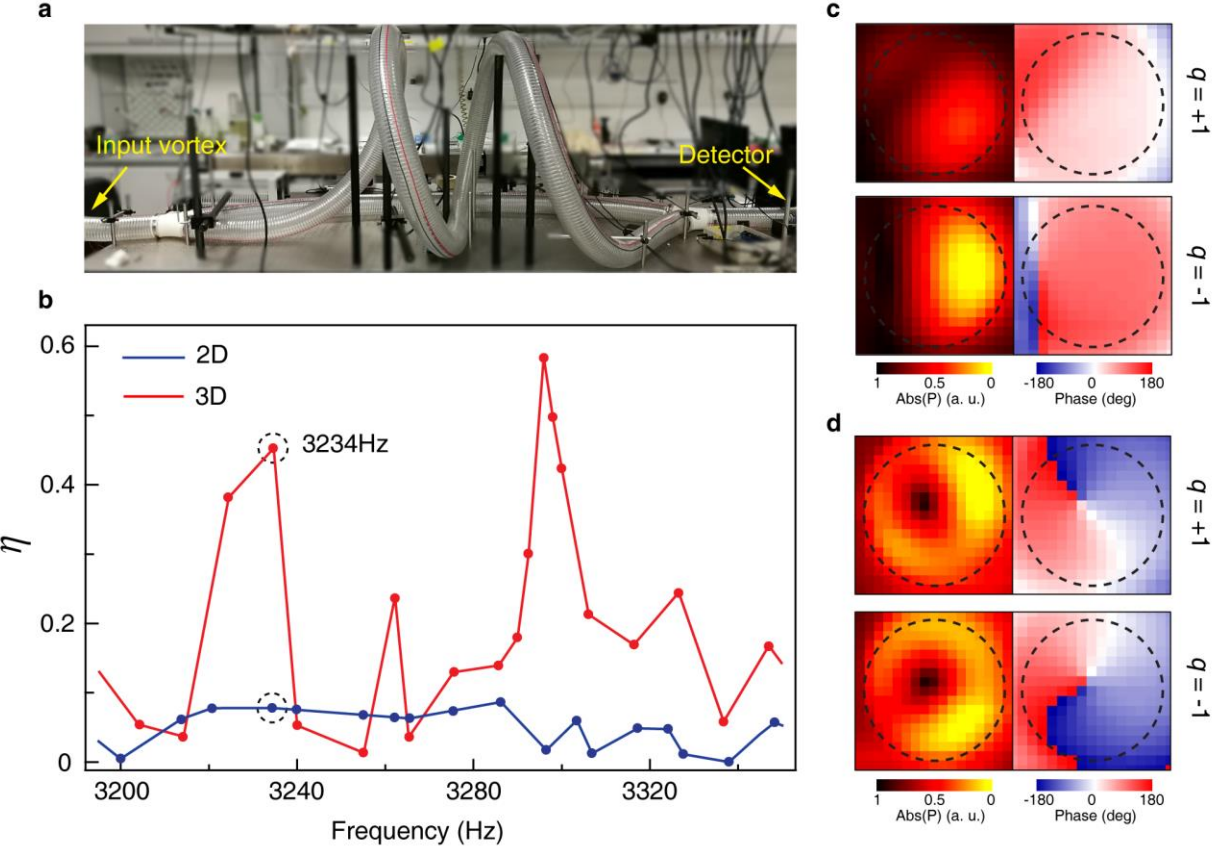
¹*Department of Physics, The Hong Kong University of Science and Technology, Hong Kong, China*

²*Department of Physics, City University of Hong Kong, Hong Kong, China*

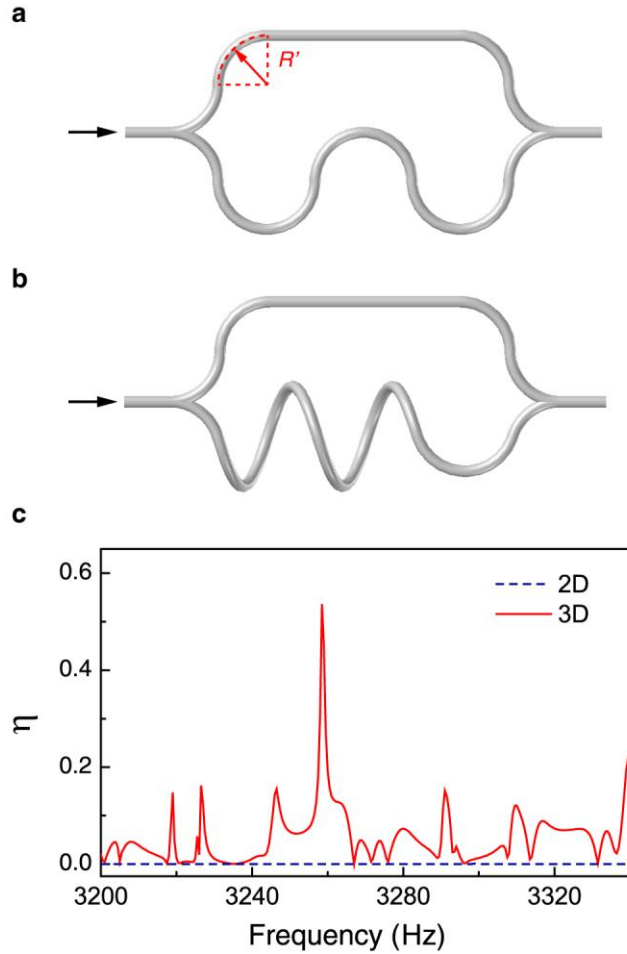
* Correspondence to C. T. Chan (phchan@ust.hk)



Supplementary Figure 1 | Band structures for helical waveguides with different pitch. The circles denote the full-wave simulation results while the solid lines denote the analytical results, which are obtained by folding the band dispersion of equation (3) into the first Brillouin zone using the mapping of $k = (D / S)k_B$. Here, we make approximations and set $S = \sqrt{D^2 + (2\pi R)^2}$.



Supplementary Figure 2 | An acoustic interferometer based on geometric phases. **a**, A 3D acoustic interferometer consisting of a helical waveguide and a bent waveguide. **b**, The transmission contrast η (see main text for definition) of the $q = \pm 1$ vortices as a function of frequency for the 2D (not shown) and 3D interferometers. The 2D setup is obtained by unwinding the helical waveguide so that the two waveguide branches lie on a 2D plane. **c**, The normalized magnitude and the phase of the output pressure field of the $q = \pm 1$ vortices at the frequency $f = 3,234$ Hz for the 3D case. **d**, The normalized magnitude and phase of the output pressure field of the $q = \pm 1$ vortices at the frequency $f = 3,234$ Hz for the 2D case, which has mirror symmetry.



Supplementary Figure 3 | Full-wave simulations of acoustic interferometers based on geometric phases. The configurations of the 2D and 3D interferometers are shown in **a** and **b**, respectively, where the $q = \pm 1$ vortices are excited at the left end. The arc parts of the waveguide in both **a** and **b** have radii of $R' = 34$ mm. The helical part has radius R and pitch D with the same values as in the experiments. **c**, The simulation results of the transmission contrast η for the 2D and 3D interferometers.

Mapping between waveguide dispersion and band structure

To verify our analytic theory, we perform comparisons between the analytical results and full-wave simulation results for the dispersion relations of the vortex modes in the helical waveguide. In the numerical simulations, the band structure is calculated by using one pitch of the helical waveguide and setting periodic boundary conditions on both ends. The analytical results are given in equation (3) of the main text. For comparisons, we fold the analytical dispersion lines back into the first Brillouin zone. This involves a mapping between the guided wave number k and the Bloch wave number k_B : $k = (D / S)k_B$, which is given by the condition that the waves undergo the same change of phase when propagating through one pitch of the helical waveguide. Here, D is the pitch and S is the total length of the helical waveguide for one pitch. In the limit of $a \ll R, D$, we have

$S \approx \sqrt{D^2 + (2\pi R)^2}$. However, for practical parameters used in the experiments and simulations, this relation is only approximately true. Supplementary Figure 1 shows the comparisons for helical waveguides of different pitch D , where we set $a = 3.25$ cm and $R = 32.5$ cm. The circles denote full-wave simulation results while the solid lines are analytical results obtained by direct use of $S = \sqrt{D^2 + (2\pi R)^2}$. Such an approximation lead to deviations between the analytical and numerical results, as in the case of $D = 65$ cm. As D increases, the analytical results gradually approach the numerical results. The black circles denote the band of the monopole mode, which is not of interest.

To obtain accurate values of S for the cases that do not fulfil the condition $a \ll R, D$, we first determine the centre frequency as $\omega = (\omega_+ + \omega_-)/2$, where ω_{\pm} denote the numerical results for the frequency of the $\pm q$ mode. This essentially gives the band structure of the corresponding straight waveguide. By fitting the analytical expression for the dispersion relation of the straight

waveguide, i.e., $\omega = c\sqrt{k_r^2 + k^2}$, to this centre frequency band structure, we obtain the correct values of S , which can be used for the mapping of $k = (D / S)k_B$. The results in Fig. 2b of the main text are obtained in this way.